

PAPER

## Research at Varian on applied superconductivity for proton therapy

To cite this article: A Godeke *et al* 2020 *Supercond. Sci. Technol.* **33** 064001

View the [article online](#) for updates and enhancements.






**IOP | ebooks™**

Bringing together innovative digital publishing with leading authors from the global scientific community.

Start exploring the collection—download the first chapter of every title for free.

# Research at Varian on applied superconductivity for proton therapy

A Godeke<sup>1</sup> , L Alberty<sup>1</sup>, E Akcöltekin<sup>1</sup>, R Babouche<sup>1</sup>, C Detourbe<sup>1</sup>, R Nast<sup>1</sup>, Ch Radermacher<sup>1</sup>, H Röcken<sup>1</sup> , A Roth<sup>1</sup>, M Schillo<sup>1</sup>, P vom Stein<sup>1</sup>, M Walpole<sup>1</sup>, J Wittschen<sup>1</sup>, K Hayashi<sup>2</sup>, E Shizuya<sup>2</sup>, H J G Krooshoop<sup>3</sup>, R Lubkemann<sup>4</sup>, A Nijhuis<sup>3,4</sup> , C H Vermeer<sup>4</sup>, W A J Wessel<sup>3</sup>, J Krause<sup>5</sup>, J Wiezoreck<sup>5</sup>, A Otto<sup>6</sup> and L Saraco<sup>6</sup>

<sup>1</sup> Varian Medical Systems Particle Therapy GmbH, Mottmannstraße 2, 53842 Troisdorf, Germany

<sup>2</sup> Sumitomo Electric Industries, Ltd, 1-1-3, Shimaya, Konohana-ku, Osaka 554-0024, Japan

<sup>3</sup> University of Twente, P.O. Box 217, 7500 AE Enschede, The Netherlands

<sup>4</sup> Foundation SuperAct, Marterstraat 66, 7559 AJ Hengelo, The Netherlands

<sup>5</sup> ECO 5 GmbH, Bornheimer Straße 33b, 53111 Bonn, Germany

<sup>6</sup> Solid Material Solutions, LLC, 55 Middlesex St, Suite 205, N. Chelmsford, MA 01863, United States of America

E-mail: [arno.godeke@varian.com](mailto:arno.godeke@varian.com)

Received 28 November 2019, revised 5 February 2020

Accepted for publication 16 March 2020

Published 24 April 2020



## Abstract

Proton therapy is a rapidly increasing modality to treat cancerous tumors, but large-scale implementation, and therefore widespread availability for patients, is hindered by the size and upfront investment for treatment facilities. Superconducting technology can enable more compact, and therefore more affordable treatment systems, by increasing the magnetic field in the magnets for the proton accelerator (typically a cyclotron) and in the beam guidance up, over, and into the patient (the gantry). In this article, we discuss research at Varian Medical Systems Particle Therapy GmbH on various superconducting technologies for potential application in future, more compact cyclotrons and gantries. We discuss which technologies are feasible, and to what extent. We demonstrate why certain conductor choices are made, and show the development of novel new conductor and magnet technologies that will be required to enable the next generation of cryogen-free, conduction-cooled compact treatment systems. We conclude that superconductivity is certainly required for the next generation of proton treatment systems, but also that the amount of compactness that can eventually be achieved is not solely determined by the magnetic field strength that is generated in the magnets.

Keywords: superconductors, medical accelerators, proton therapy, gantry, cyclotron, conduction cooling

(Some figures may appear in colour only in the online journal)

## 1. Introduction

One in eight deaths worldwide was caused by cancer in 2007, and in 2018 this had increased to one in six deaths worldwide, according to the Global Cancer Facts & figures publications of 2007 and 2018 [1, 2]. Cancer was the second-leading cause of death (following cardiovascular diseases) worldwide in 2018. The predicted number of global new cancer cases was 12 million in 2007, and this number increased to 17 million in 2018. In 2007, 27 million new cancer cases were predicted to occur

in 2050, but by 2018 that was adjusted to occur already in 2040. These chilling numbers and growth clearly identify a need for improved modalities to treat cancer. Naturally, the best solution for cancer is prevention, but unfortunately, the numbers above show that a growing and aging global population outruns awareness and increasing life standards.

The primary modalities of cancer treatment are surgery, chemotherapy, and radiotherapy, which may be used alone or in combination [1]. The most common radiation treatment is with high energy photons (i.e. x-rays), and a typical dose

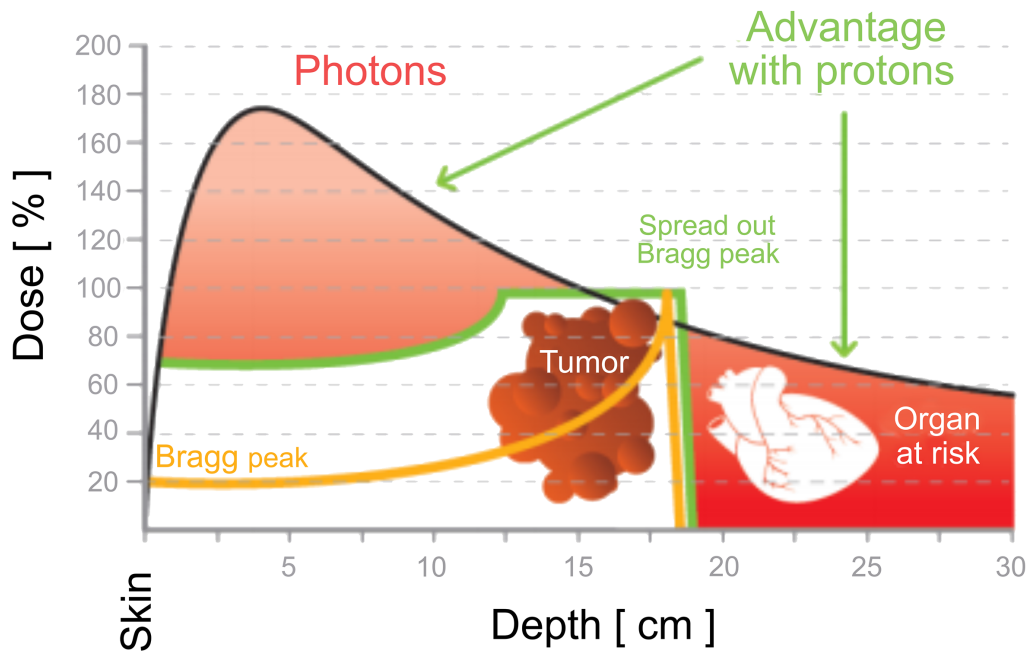


**Figure 1.** Comparison of the deposited dose distributions when treating cancerous tissue with photons or protons.

distribution as a function of depth in the body is shown in figure 1. It is clear that a larger fraction of the radiation dose is deposited outside the tumor in the patient's body, which is damaging to the healthy tissue and also introduces the risk for secondary cancers to occur. The treatment is therefore mostly administered from multiple angles, in order to reduce the dose in areas outside the target and deposit the largest overall dose in the tumor.

In contrast, when high energy protons enter the body, they interact with the tissue, which causes them to lose energy and slow down, after which they lose an increased amount of energy per penetration depth, and slow down faster, eventually resulting in a complete stop where the largest amount of energy is deposited. This behavior is referred to as the occurrence of a Bragg peak, and its depth inside the body is a function of the initial energy of the protons. By varying the energy of the protons, a spread-out Bragg peak results, which can be tailored across the tumor extent in depth. Further accuracy in dose deposition is achieved by scanning the focused proton beam across the tumor cross-section for each given proton energy, i.e. treatment depth, which is referred to as pencil beam scanning.

From figure 1 it is seen that a treatment with protons results in roughly half of the radiation dose before the tumor, with no affected tissue behind the tumor. This is specifically beneficial for head and neck treatments and for pediatric patients, and results in less side effects and secondary cancers when compared to a treatment with photons. A treatment with protons is further commonly also administered from multiple angles by rotating the gantry around the patient, thereby further increasing the ratio of the deposited dose in the tumor versus the one in the healthy tissue.

The typical layout of a multi-room proton treatment facility is shown in figure 2. Protons are accelerated to a fixed energy

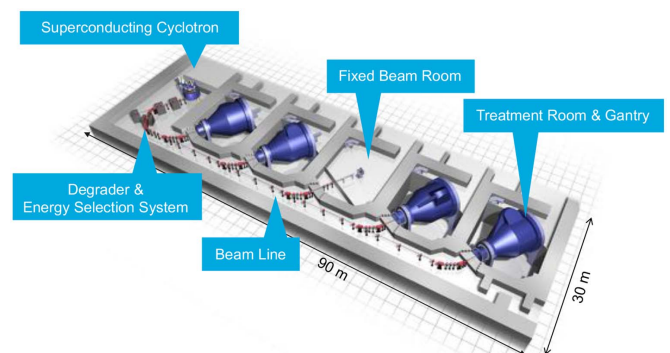


**Figure 2.** Artist impression of a multi-room proton therapy treatment facility.

in a cyclotron. Varian's AC250 isochronous cyclotron can generate a continuous 800 nA beam of protons with an energy of 250 MeV, which corresponds to a penetration depth of 37 cm in water, i.e. sufficient depth to fully penetrate a human body. A degrader and energy selection system after the cyclotron varies the beam energy typically between 70 to 230 MeV, after which the protons enter the beam-line towards a selected gantry. The gantry then guides the beam up, over, and into the patient, and the gantry can be rotated over  $360^\circ$  in the case of Varian's ProBeam<sup>®</sup> and ProBeam 360<sup>®</sup> solutions. Located just before the patient is a nozzle, which contains scanning magnets, a dose and position monitor, and an imaging system, thereby completing the beam trajectory. In multi-room facilities, patients can be prepared in one room, while active treatment takes place in another room, utilizing the accelerator to the fullest. Fixed beam rooms without lateral beam-scanning, for example for eye treatments, are also available.

A key problem for the large-scale implementation of proton-therapy is immediately evident for a multi-room



**Figure 3.** Artist impression of Varian's single-room ProBeam<sup>®</sup> proton therapy solution.

treatment facility: The 5-room installation as shown in figure 2 has a footprint of about 30 m by 90 m, which leads to significant upfront investments for such facilities. To limit the initial investment, one can choose to install a single-room system, for which an artist's view is shown in figure 3, with a cross-sectional sideview in figure 4. It is seen that single-room treatment facilities, such as Varian's ProBeam<sup>®</sup> Compact solution introduced in 2014, and the more compact (but lower beam energy) ProBeam 360<sup>°</sup> proton therapy solution introduced in 2019, with their approximately 8 m diameter gantries, are still large compared to other modalities, while the ProBeam 360<sup>°</sup> design is already at the limit of what can be achieved with resistive gantry magnet solutions. Other single-room solutions (see e.g. the review in [3]), such as Mevion Medical Systems' S250<sup>TM</sup> (2012) and S250i<sup>TM</sup> (2018) systems, as well as Ion Beam Applications' (IBA) Proteus<sup>®</sup> One (2014) and Hitachi's Single Room Solution (2018), also remain very large when compared to photon treatment systems (figure 4).

In 2018 there were 199 proton treatment rooms available globally [4]. Assuming that 60% of the annual cancer patients will receive radiation treatment, and that of those who receive radiation treatment 20% would benefit from protons, then at the present throughput of 300 patients per room and year, it follows that in 2018, with 17 million new cancer patients [2], there was a global need of 6 800 rooms. This means that less than 3% of the cancer patients that would have benefitted from protons in 2018 had access to treatment. When observing the 27 million new cancer patients as predicted in 2018 for 2040 [2], a global need of more than 10 000 rooms emerges. Assuming an average of two rooms per system, it follows that there is a need to deliver 250 systems annually for the coming 20 years.

Although these demands for proton-therapy systems seem huge, they have far from materialized: Over the past 10 years since proton therapy was added to its product portfolio, Varian has committed to a little more than 80 proton treatment rooms, or 8 rooms annually on average. When comparing these numbers to cancer treatment with photons for illustration: Varian has an installed base of more than 8 000 medical linear accelerators, i.e. a factor 100 more. In figure 4, a size comparison is made between Varian's state-of-the-art proton therapy solutions and the vault size for a TrueBeam<sup>®</sup> photon solution. From this comparison it seems that to get anywhere near to fulfilling the desired amount of system implementations, significant size, and thereby cost, reductions will be needed, and superconducting technologies are required to realize this.

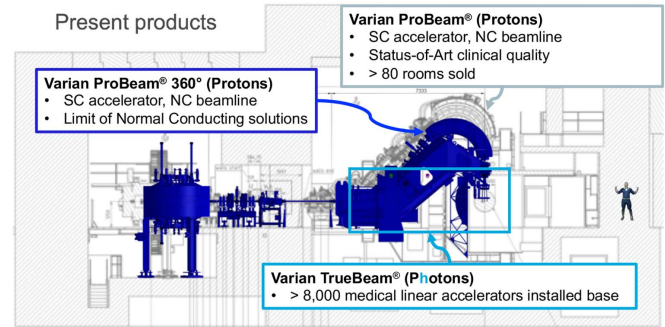


**Figure 4.** Size comparison between Varian's ProBeam<sup>®</sup> and ProBeam 360<sup>°</sup> proton therapy solutions, and the vault size for Varian's TrueBeam<sup>®</sup> photon treatment solution.

Ideally, such technologies are cryogen-free. The reason for this is obvious for rotating systems such as gantries, but also for static systems such as a cyclotron there are arguments for a cryogen-free technology: Cryostat construction is simplified, potential on-site handling of cryogenic liquids is prevented, and only one superconducting technology and conductor is needed for the entire system.

## 2. Superconducting magnets

The magnetic flux density  $B$  that is required to bend a charged particle with mass  $m$ , velocity  $v$ , momentum  $p$  and charge  $q$  over a radius  $\rho$ , is given by

$$B\rho = \frac{mv}{q} = \frac{p}{q}. \quad (1)$$

The term  $B\rho$  is usually referred to as the 'magnetic rigidity' of a beam in [Tm]. Since protons with a kinetic energy of 250 MeV travel at 61% of the speed of light  $c$ , their momentum is most commonly calculated by using a relativistic energy balance for the total energy

$$E_{\text{total}} = mc^2 = c\sqrt{p^2 + m_0^2c^2}, \quad (2)$$

in which the first term represents the kinetic energy, and the second term represents the proton's rest energy for its mass-at-rest  $m_0$ . By combining equations (1) and (2) it follows for the magnetic rigidity

$$B\rho = 2.432 \text{ Tm}, \quad (3)$$

for protons with a kinetic energy of 250 MeV.

Relation (3) is plotted in figure 5, together with the limiting magnetic fields for resistive dipole magnets and for record low temperature superconducting Nb<sub>3</sub>Sn magnets [5]. It is immediately evident that the maximum gain in bend radius, when switching from resistive to superconducting magnet technology, is only about 1 m. It is also clear from figure 5 that the relative gain in bending radius becomes increasingly less, while the dipole magnet technology becomes increasingly complex. An optimum dipole magnetic field seems to be located around

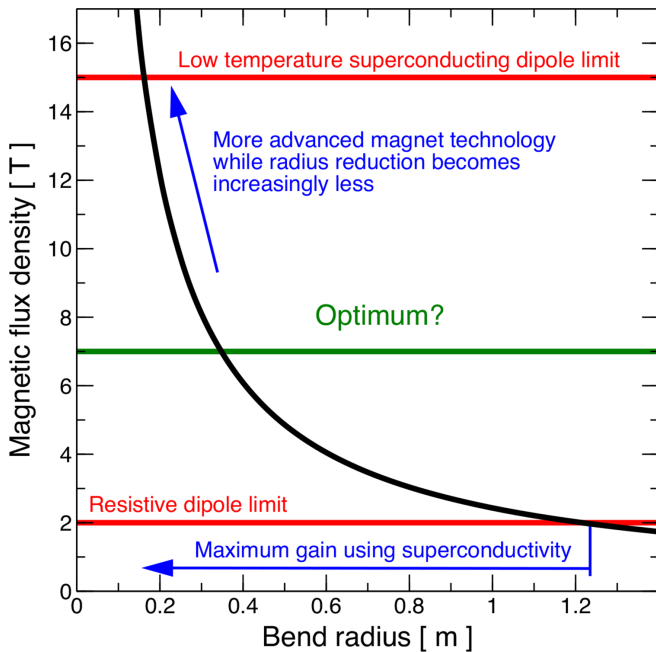


**Figure 5.** Required magnetic flux density to bend 250 MeV protons within a given radius. The magnetic field limitations for resistive and low temperature superconducting dipole magnets, and the resulting maximum radius reduction when using superconducting magnets, are also shown.

7 T: Most of the reduction in bending radius is realized at this field, but the magnet technology is still not too complex and repetitively proven [6], albeit for straight, not strongly curved dipoles.

Varian's AC250, which uses Nb-Ti main coils, has a central magnetic field of only 2.4 T, and an outer diameter of just over 3 m. For the main solenoids in a future, more compact, isochronous cyclotron it can be argued that, similar as for a bend magnet in a gantry, a central cyclotron magnetic field of around 5 T (i.e. around 7 T at the superconducting windings), is optimal. One can certainly make a set of split solenoids that generate a central magnetic field of significantly more than 5 T using existing technology, thereby reducing the cyclotron diameter more. It will, however, be difficult, if not impossible, to also fit the RF components, the cryogenics, the flutter field generating components (see section 4), and the load bearing components in the available volume. Hence, a magnetic field at the superconductors on the order of 5 to 7 T seems optimum both for bend magnets in gantries, as well as for isochronous cyclotrons, which yields a simplification when a conductor type and technology needs to be selected, since one superconducting technology can be used for the entire system.

### 3. Superconducting bend magnets for gantries

We studied the feasibility of superconducting final bend magnets for gantries in collaborations with the Paul Scherrer Institute in Villigen, Switzerland (PSI), and with Lawrence Berkeley National Laboratory in Berkeley, CA, USA (LBNL). In both studies, the high performance of superconducting

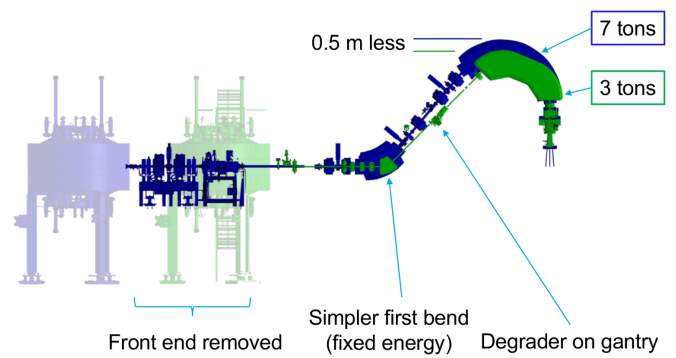


**Figure 6.** Artist impression of potential size reductions when replacing a resistive main bend magnet in a gantry by a superconducting version with a large momentum acceptance.

magnets was utilized to design large-bore achromatic magnets for the final bend in a gantry, with a higher momentum acceptance than what is possible with resistive magnets. In this way, a treatment can be performed with one, two, or at maximum three magnetic field settings, depending on the proton energy range that is required for the treatment. Limiting the need to ramp the magnet results in increased patient throughput and faster dose delivery, which is beneficial for organ motion mitigation and emerging modalities such as FLASH [7]. The need for magnetic field changes obviously also needs to be limited as much as possible due to undesirable losses in the superconducting material, which will cause the temperature to increase in a conduction-cooled magnet configuration. An important advantage of an achromatic final bend magnet is that the degrader can be placed on the gantry in between the first and the final bend magnet, as opposed to a placement before the gantry. Moving the degrader onto the gantry enables a shorter system, as is sketched in figure 6.

In the collaboration with PSI, a final bend magnet was studied that consisted of two sets of double racetrack dipoles with quadrupole magnets for focusing before, in between, and after the double racetrack sets [8–12]. The design philosophy focused on the utilization of proven magnet design concepts, using comparatively easy to manufacture coils. Cryogen-free, conduction-cooled designs with and without iron, and using Nb-Ti and Nb<sub>3</sub>Sn superconducting cables were investigated. Feasible solutions with acceptable particle tracking were found with maximum magnetic fields at the conductors of 7.5 T without iron and 5.7 T with iron, and temperature margins on the order of 5 to 6 K for Nb<sub>3</sub>Sn and 1.5 K for Nb-Ti, but no hardware has been manufactured so far. In a more recent further optimized design for a gantry bend magnet the energy acceptance has been increased to  $\pm 30\%$  [12].

In the LBNL effort, a combined function, achromatic final bend magnet was studied, using a Nb-Ti, four-layer 'Canted-Cosine-Theta' (also referred to as 'Double-Helix') design [13–15]. The design philosophy focused on an elegant solution while exploring new magnet technology concepts. Two inner layers in this design form a focusing-defocusing quadrupole magnet, and two outer layers form a bending dipole. A feasible design with acceptable particle tracking was

**Table 1.** Advantages and disadvantages of a superconducting final bend magnet for a gantry compared to a resistive solution, assuming no overall cost difference.

Advantage	Disadvantage
Smaller radius	Radius reduction limited
Lighter magnet	More complex (risk)
Smaller building footprint	Cryogenics
<i>Energy variation</i>	<i>Energy variation</i>

found with a maximum magnetic field on the conductor of 5.2 T and a temperature margin of 1.3 K. Much of the LBNL effort focused on the practical implementation of an elegantly simple solution, but the design proved difficult to manufacture. Eventually, a large demonstration dipole was fabricated and tested with varying degrees of success [16].

The key outcomes of these studies are summarized in table 1, while in figure 6 a size comparison is shown between Varian's most compact resistive gantry solution, ProBeam 360<sup>®</sup>, and a gantry solution that includes the PSI bend magnet design. Preliminary cost estimates suggest that the additional cost of the cryostat and superconducting material are offset by the lower weight of the magnet and thus savings in the gantry support structure, by the simpler first bend magnet that only has to transport a single energy beam, and by the removal of the front end. The actual cost savings are in the smaller building footprint and the likely lower energy-consumption of a superconducting variant. The energy variation is both an advantage and a disadvantage: The magnetic field does not have to continuously change with the beam energy, as for a resistive solution, but due to the losses it is a disadvantage when the magnet has to be ramped to a different magnetic field.

Overall it is evident that, despite the advantageous reduction in building footprint, the radial reduction in size is not very large, as was clear also from figure 5. The reason for this is that the diameter of a traditional gantry layout is largely driven by the required space for the nozzle equipment and the required distance between the scanner and the patient, which are both on the order of 1 to 2 m, to which the height of the final bend magnet will be added. Simply switching to a superconducting magnet is therefore insufficient to make truly significant reductions in size, and other configurations for the beam optics need to be considered to obtain further size reductions.

A larger diameter reduction can be achieved with superconducting magnets in a gantry for carbon therapy, due to the approximately factor 3 larger beam stiffness. This becomes evident when comparing the normal conducting Heidelberg gantry at GSI in Germany at 13 m diameter and a weight of 675 ton [3, 17], to the superconducting gantry at the National Institute of Radiological Science in Japan at just under 11 m diameter and a weight of 300 ton [18].

Non-traditional gantry designs with modified optics configurations are a continuing area of research (see e.g. the discussions in [10]). Many utilize the larger energy acceptance (achromaticity) that is possible with superconducting magnets, thereby enabling a degrader on the gantry (figure 6)

and/or upstream scanning [10] or more exotic designs such as Fixed Field Alternating Gradient structures [19]. What can lead to truly compact gantries, however, still is not clear. The current main benefit of gantries with superconducting magnets is weight reduction, as is for example studied for figure 6 and demonstrated in the ProNova SC360 superconducting gantry [20] which, at 25 ton, is a factor 4 to 8 lighter than the traditional normal conducting versions.

## 4. Compact isochronous cyclotrons

### 4.1. Magnet requirements

The most compact and cost-efficient way to accelerate protons to the required energy levels in the range of 200 to 250 MeV is by using a cyclotron to accelerate the ions. When using only normal conducting technologies, cyclotrons are large (> 4 m in diameter) and heavy (around 200 tons). Varian's AC250 (see figure 7(a) and (b)) was the first particle therapy cyclotron manufactured in a commercial setting that utilized superconducting technology to generate the main solenoid magnetic field. This magnetic field, which increases non-linear with radius to compensate for the relativistic mass increase of the protons (figure 7(c)), opposes the centripetal force that accelerated protons experience, thereby keeping the protons in an azimuthal track inside the cyclotron. At just over 3 m in diameter, and with a weight of around 90 tons, Varian's AC250 is significantly more compact and lighter than conventional cyclotrons, thereby demonstrating the gains that can be achieved when using superconducting technology.

Isochronous cyclotrons, such as AC250, are able to generate a continuous high-current proton beam, which is key to fast patient throughput and modern treatment modalities such as FLASH [7]. A specific complication when designing an isochronous cyclotron (as opposed to synchro-cyclotrons, such as in Mevion's SC250 system and IBA's S2C2), is the need for a beam-focusing alternating magnetic field (or 'flutter' field) along the beam trajectory (figure 7(c)), without which the accelerating beam becomes unstable. For AC250, this alternating magnetic field is generated through ferro-magnetic (iron) 'hills' and 'valleys' that work as magnetic lenses to superimpose on the main field into the desired azimuthally alternating maxima and minima.

From figure 5 and equation (3) it follows that to construct more compact cyclotrons at a smaller radius, a higher magnetic field is needed. For synchro-cyclotrons this poses not an issue, and is a matter of using appropriate superconductors and magnet engineering to design a higher magnetic field solenoid. For isochronous cyclotrons, however, increasing the magnetic field means that the iron that generates the flutter field will saturate. This leads to a requirement for superconducting flutter coils that can replace the iron pole-pieces to generate the flutter field.

Various designs can be proposed for the shape of such flutter coils. The optimal shape is, however, driven by achieving all critical beam dynamics parameters [31] for a given magnet size, beam extraction energy and beam extraction efficiency. This typically results into 'kidney' shaped hills and valleys of

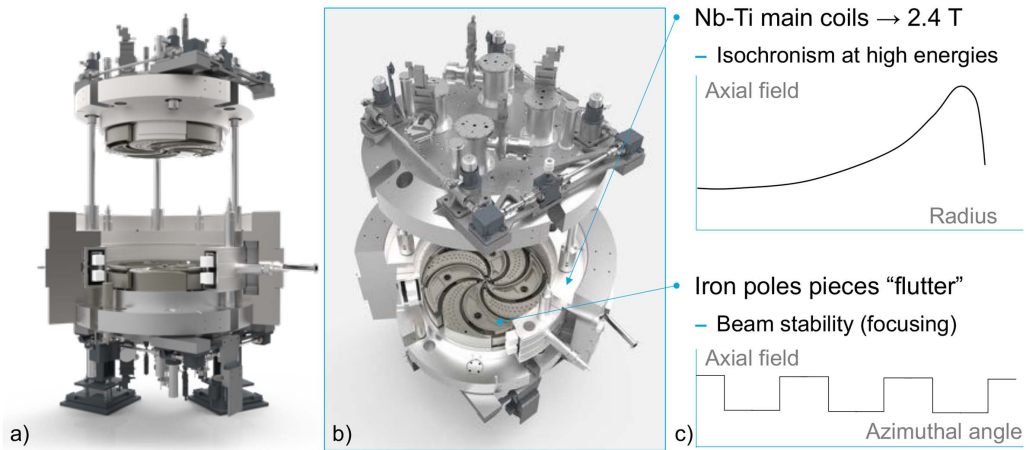


**Figure 7.** Artist impression of Varian’s AC250 isochronous superconducting cyclotron. (a) Open side view with a cut-away; (b) Open top-view with a cut-away depicting the iron hills and valleys that generate the flutter magnetic field; (c) Sketches of the ideal axial magnetic field as a function of radius and azimuthal angle, which are superimposed within the cyclotron to guide the beam while simultaneously providing beam focusing.

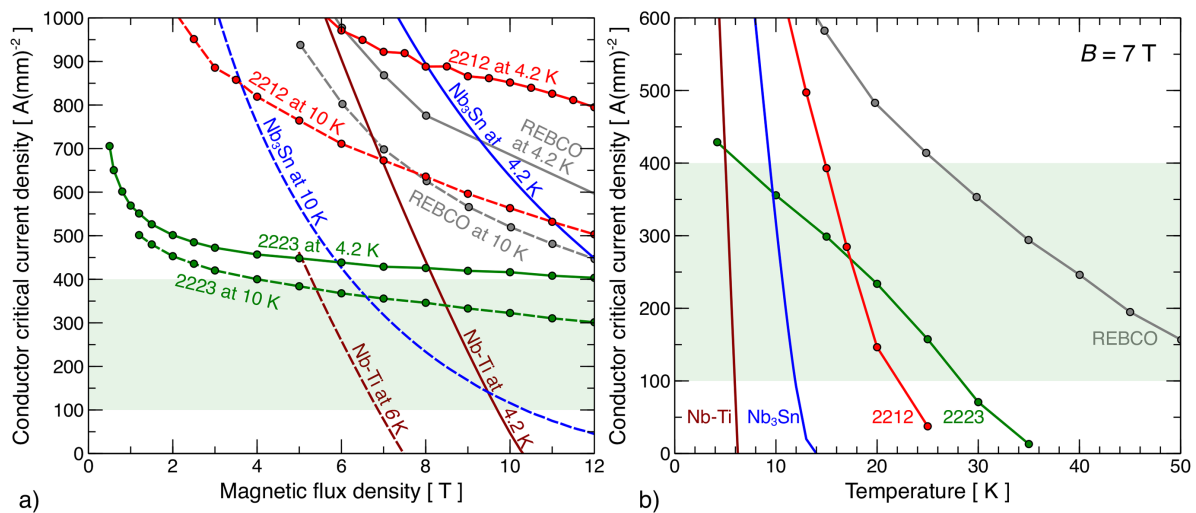


**Figure 8.** (a) Conductor critical current density as a function of magnetic field for commercially available Nb<sub>3</sub>Sn [21–23], Bi-2223 [24–26], Bi-2212 [27], and REBCO [28] at 4.2 K and 10 K, and Nb-Ti [29, 30] at 4.2 K and 6 K. (b) Conductor critical current density at  $B = 7$  T as a function of temperature for the same superconductors. The shaded areas depict the range of current densities that are common in superconducting magnet applications.

the iron, as shown in figure 7(b). In addition to such rather complex flutter coils, also a split-pair solenoid would need to be designed, with a magnetic field that is approximately twice the 2.4 T central magnetic field of AC250. Obviously this leads to much higher demands on the selected conductor, and with the magnetic field, the Lorentz loads will increase significantly. The flutter coils and higher performance split-solenoid main coil lead, in combination with a desire to have a cryogen-free conduction-cooled system, to non-trivial magnet technologies.

#### 4.2. Conductor options

Cryogen-free conduction-cooled magnet systems can be constructed using Gifford-McMahon cryocoolers that have a cooling capacity of 1.5–2.0 W at 4.2 K at their second stage. At

10 K, the cooling power of the second stage of such coolers increases to just below 15 W, i.e. they can provide about one order of magnitude more cooling power at 10 K. This, combined with increases in heat-capacity of the materials, makes it highly desirable to operate conduction-cooled systems at temperatures above 4.2 K. Operating magnets around 10 K further makes the more expensive high temperature superconductors (HTS) more competitive, because the higher conductor cost compared to the low temperature superconductors (LTS) can be balanced against savings in cooling cost, since cryocoolers are also high-cost items.

In figure 8(a) a summary is given of the conductor critical current densities as a function of magnetic field at 4.2 K and 10 K for commercially available superconductors. It should be emphasized that the current density values in figure 8 are overall conductor current densities, which are often referred to as

engineering current densities ( $J_E$ ). The current density values for REBCO are, for this reason, much dependent on the thickness of the copper layer that is applied around the conductor for electrical stability reasons.  $MgB_2$  is not included, since it is not competitive in terms of current density with high performance Nb-Ti in the magnetic field range of interest. For Nb-Ti, a parameterization [30] of the critical current density at 4.2 K and 6 K is shown instead of 4.2 K and 10 K, since its critical temperature ( $T_c$ ) at zero magnetic field is only 9.2 K, and this reduces further to just above 6 K at  $B = 7$  T. The data shown is for record Nb-Ti wire as used for CERN's MSFISC record dipole magnet [29] which, at  $1,160 \text{ A}(\text{mm})^{-2}$  at 5 T and 4.2 K, is slightly better performing than standard wire (carrying  $1,000 \text{ A}(\text{mm})^{-2}$  [32]) that was used for the Large Hadron Collider ring dipole magnets. Ternary Nb-Ti-Ta has a critical current density that is shifted 0.5 to 1 T towards higher magnetic field compared to binary Nb-Ti, thereby providing a 0.5 to 1 K increase in temperature margin and thus rendering it an attractive alternative, but it is no longer readily available. The  $Nb_3Sn$  data is an ITER production parameterization [22, 23] of ITER quality Internal-Tin wire that was manufactured by Luvata [21]. The critical current density of high performance  $Nb_3Sn$  can be up to a factor three higher, but at a substantially higher cost, whereas ITER quality conductor carries sufficient current and has finer filaments and therefore lower losses during magnet ramping, as well as improved electrical stability.

For the high-temperature superconductors Bi-2223 and REBCO, the worst-case critical current density is shown, i.e. as a function of magnetic field that is perpendicular to the tapes. It should be emphasized that the performance shown in figure 8 for Bi-2212 is for wire that was reacted under overpressure, whereas the current density for Bi-2212 that is reacted without overpressure is approximately a factor three lower. The factor three increase through an overpressure reaction is less than the factor seven that is claimed by others [33], but stems from a comparison between coil witness samples that were reacted at 1 bar, for which a maximum critical current of 100 A (or  $199 \text{ A}(\text{mm})^{-2}$ ) at 15 T and 4.2 K was measured [34], and samples for a strain experiment that were reacted at 100 bar overpressure, and for which a maximum critical current of 360 A (or  $716 \text{ A}(\text{mm})^{-2}$ ) at 15 T and 4.2 K was measured [35].

The shaded areas in the graphs further indicate the range of common current densities at which conductors operate in superconducting magnets: A conductor's potential is not explored to its full capacity below  $100 \text{ A}(\text{mm})^{-2}$ , while protection becomes problematic above  $400 \text{ A}(\text{mm})^{-2}$ .

Overall, it is found that all the available conductors, except Nb-Ti, fulfill the current density requirements around the 7 T magnetic field of interest, and this also holds at temperatures approaching 10 K. Nb-Ti, however, has only a temperature margin on the order of 1 K when operated at 4.2 K at the same magnetic field. This means that the thermodynamic layout of a conduction-cooled system has to be exceptionally well designed when Nb-Ti is used. The actual temperatures that will be achieved in a complex system are, however, hard to predict due to variations in the quality of the thermal connections that

depend strongly on how well they are designed and executed. This uncertainty is unacceptable for a series-produced cyclotron, since the system will not work if the design magnetic field is not reached as a result of coil components being, say, 1 K higher than they were designed for.

A more interesting comparison to down-select the conductor options appears when the critical current densities are plotted as a function of temperature at the magnetic field of interest, i.e. at  $B = 7$  T, as is done in figure 8b. It is immediately evident that Nb-Ti cannot be used at a target temperature around 10 K. It is also clear that although  $Nb_3Sn$  could be used at, say, 8 K, it will have a limited temperature margin. Furthermore, one still has to react  $Nb_3Sn$  at temperatures above  $600^\circ\text{C}$ , and therefore cope with a limited material set that can handle such temperatures. This is specifically true for the conductor insulation, for which glass fiber is commonly used, which is coated with seizing to limit abrasion. This seizing burns off during the heat treatment after which the insulation is fragile, and the burning of the sizing additionally causes carbon deposits into the windings. Heat treatments for large production quantities, which will involve the reaction of multiple coils at once, also create a risk due to potential errors during the process.

Alternatively, one could prevent the need for heat-treatment by using pre-reacted  $Nb_3Sn$ , which has more recently become commercially available and has been successfully proven in magnets [36]. For the main coils of a compact cyclotron, which will have a diameter on the order of a meter, pre-reacted  $Nb_3Sn$  cable is certainly attractive, and the same might be true for bend magnets for gantries. For flutter coils, however, in which the conductor needs to bend in two directions (see section 4.3) it is probable that the opposite bend directions will consume too much of the available strain space in pre-reacted  $Nb_3Sn$ . In addition, it can be desirable to select only one conductor technology.

The three HTS conductors can all comfortably carry the required current densities at the desired magnetic field and temperature. REBCO and Bi-2212 are, however, at the time of writing, at least a factor two more expensive than Bi-2223. For Bi-2212, one has to additionally account for a reaction heat-treatment that is significantly more difficult than for  $Nb_3Sn$ , and handle even more stringent material compatibility issues, due to the need to heat-treat the coils in an oxygen-rich environment.

REBCO has a very large current density capacity, although the magnitude depends strongly on the thickness of the copper plating. The large temperature margin is good for stability, but it also makes it harder to protect as a result of a slow normal zone propagation velocity. Another potential issue with REBCO for our application is the fact that it is a single crystal without possibilities for current sharing in case of a local defect. If local defects in the conductor are not located in the regions in a coil where the highest magnetic field perpendicular to the tape occurs, then it becomes impossible to detect that something is wrong, and the large temperature margin will only reduce the chance of detecting such a defect. The resulting outcome of a local defect can therefore be irreversible damage to the coil.



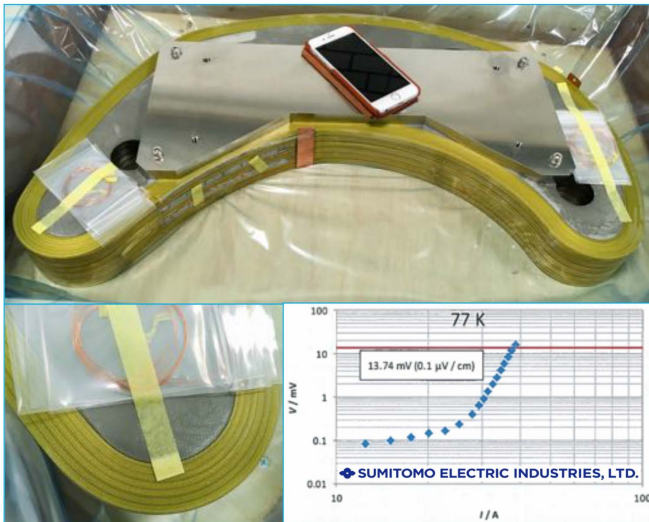


**Figure 9.** Proof-of-principle superconducting flutter coil, comprised of a stack of six Bi-2223 double-pancakes and manufactured for Varian by Sumitomo Electric Industries, Ltd. The bottom half of the picture shows a detail of the coil (left) and the voltage-current transition of the entire coil (right), measured in a liquid nitrogen bath at 77 K.

Through the discussions above we therefore down-select to Bi-2223 as our currently most favorable conductor for the magnetic field and temperature ranges of interest. It is multifilamentary (albeit without full separation and twist), and it is commercially available in large quantities and long lengths with various options of external reinforcement. With respect to the higher cost as compared to  $\text{Nb}_3\text{Sn}$ , one can argue that this can be offset against the need to react  $\text{Nb}_3\text{Sn}$  after coil winding when small bending radii are involved, which involves added cost and risk, and advantages in cooling and stability as a result of the higher critical temperature.

A suitable alternative conductor for our application would still be pre-reacted  $\text{Nb}_3\text{Sn}$ , although there are uncertainties in terms of the available strain-space for flutter coils. A combination, such as pre-reacted  $\text{Nb}_3\text{Sn}$  cable for the main coils and flutter coils manufactured from Bi-2223, is also attractive, although the potential advantage of having to handle only a single conductor technology is then lost.

#### 4.3. A prototype superconducting flutter coil

The fabrication of a coil with strongly concave windings, as is needed for kidney-shaped flutter coils, is far from trivial. Sumitomo Electric Industries (SEI), however, had already demonstrated in previous work [37], that they were able to wind curved double-pancake coils from our conductor of choice. SEI is also a manufacturer of Bi-2223 tape, and was therefore a natural partner to fabricate a flutter coil from their DI-BSCCO Bi-2223 conductor.

After detailed iterations on the coil design details, the prototype flutter coil as shown in figure 9 was successfully manufactured and tested at SEI at 77 K in a liquid nitrogen bath. It consists of six double-pancake coils that are stacked together

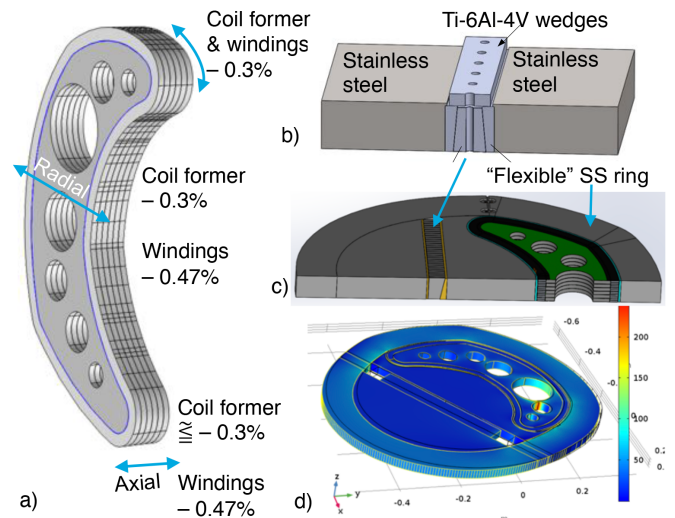


**Figure 10.** (a) Thermal contraction in various directions of the flutter coil components from room temperature down to 4.2 K, as calculated through the consideration of the individual material properties in Comsol®. (b) Ti-6Al-4 V wedges that compensate for the larger radial contraction of the windings compared to the coil former during cooldown. (c) Mechanical model of the coil-clamping structure that applies and retains a desired pre-load from room temperature to 4.2 K. (d) COMSOL® thermo-mechanical model to simulate and verify the design concepts for the clamping structure.

with copper (for thermal conductivity) and glass-fiber reinforced epoxy plates (for electrical insulation) in between them. The coil formers for the individual double-pancakes are fabricated from stainless-steel 316 L, and are coated with silicone lubricant around their circumference to prevent bonding to the winding pack during epoxy impregnation.

To achieve the ampère-turns needed for a compact cyclotron design [38], as well as a sufficient margin of about 30%, the used conductor is based on a reduced thickness DI-BSCCO Type H tape, laminated with stainless-steel 304 for reinforcement, and insulated with a double wrap of  $5\ \mu\text{m}$  polyimide tape. The magnetic field profile from a compact cyclotron design is used to calculate the dissipation (as a result of a finite  $n$ -value) along the length of the conductor at the design operating current. The total dissipation, including the soldered connections for the lead-in, lead-out, and in between the double-pancakes, per flutter coil at its projected operating current of 380 A at 4.2 K, is estimated to be 0.45 W. About 0.27 W of the total dissipated power stems from the finite  $n$ -value of the conductor. The total heat-load from the flutter coils during operation is taken into account in the thermal design of the cold mass of a compact cyclotron [38].

The fabrication and 77 K test of a first-of-its-kind HTS flutter coil was successful and lower temperature tests in conduction-cooled cryostats have been carefully analyzed (section 4.4) and designed (section 4.5).

#### 4.4. Finite element modeling

Extensive thermo-mechanical modeling of the cooldown, test, operation, and quench of the flutter coil was done by ECO 5

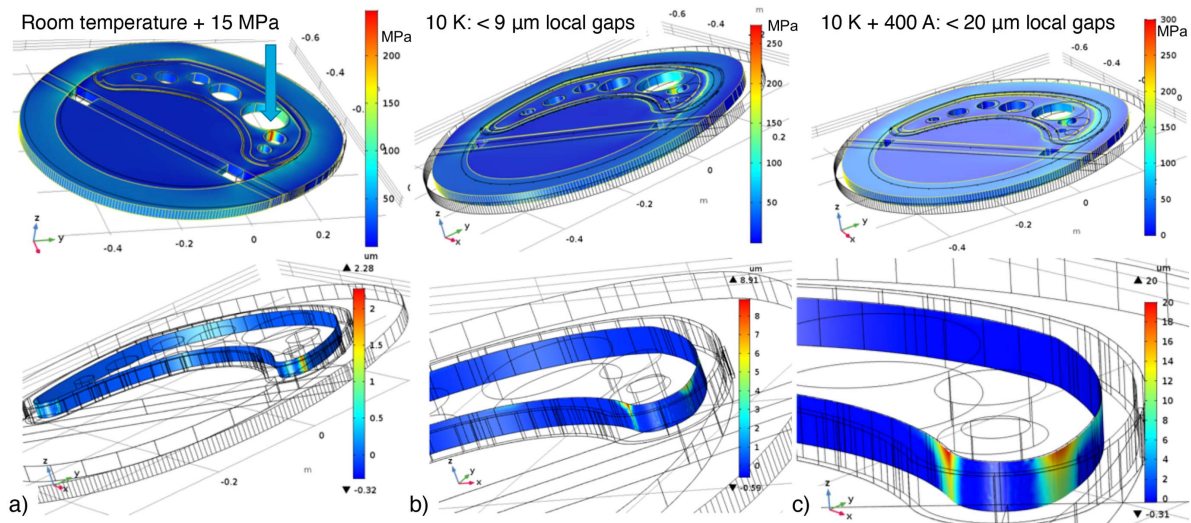


**Figure 11.** COMSOL<sup>®</sup> thermo-mechanical model of the radial clamping system at room temperature with 15 MPa pressure applied to the coil (a), after cooldown to 10 K (b), and after excitation of the coil to 400 A (c). The top figures represent the Von Mises stress on the structure, and the bottom figures represent the gap between the winding pack and the coil former. The detected local stress concentration as indicated by the arrow in the top half of (a) is mitigated by inserting a stainless-steel plug in the coil former during the test.

in Bonn, Germany, using the COMSOL Multiphysics<sup>®</sup> software [39]. This was done in order to warrant a safe design and operation during testing in self-field and when being used in a cyclotron.

Since thermal contraction and thermal conductivity data for the winding pack were not available, these were calculated in COMSOL<sup>®</sup> through consideration of the individual material properties. The resulting thermal contraction of the flutter coil components in the three principal directions is summarized in figure 10(a).

A key finding is that the winding pack, both in radial direction as well in axial direction, contracts by  $-0.47\%$  during cooldown from room temperature to 4.2 K, whereas the coil former contracts by  $-0.3\%$  in the radial direction, and slightly more contraction than  $-0.3\%$  in the axial direction. This means that after cooldown and in the radial direction, a gap will tend to occur in between the winding pack and the coil former, because the winding pack will move away from the coil former. The contraction difference will result in undesirable shear-stresses, since the copper plates in between the individual double-pancakes extend inside the winding pack for cooling purposes. The difference in thermal contraction in the axial direction results in movement of the winding pack away from a clamping structure that clamps down on the coil former, also causing a tendency for a gap to occur above and below the winding pack.

One of the philosophies in superconducting magnet design, which we adhere to here, is that the occurrence of gaps needs to be prevented, since gaps allow for undefined conductor movement, potentially causing instability and/or damage. Strictly speaking, one would not necessarily expect thermal instabilities due to small conductor displacements with high temperature superconductors, as a result of the large temperature margin (in contrast to low temperature superconductors where small energy depositions will trigger quenches). Mechanical instabilities, however, as a result of potentially

**Table 2.** Mechanical properties of hard-rolled stainless-steel 304 [40].

	Young's modules $E$ [ GPa ]	Tensile yield stress $\sigma_y$ [ MPa ]	Resulting yield strain $\epsilon_y$
Room temperature	178	1,193	0.67%
20 K	210	1,558	0.74%

damaging bending strains and undesirable shear stresses as mentioned in the previous paragraph, are dangerous and will therefore need to be mitigated. To prevent radial gaps from occurring during cooldown, and to support the coil against the Lorentz loads during a test in self-field, a stainless-steel 304 radial clamp-structure with a 'flexible' stainless-steel ring and Ti-6Al-4 V wedges was designed, as shown in figure 10(b) through (d).

The clamp system enables the application of a room temperature pre-load on the coil in radial direction using the wedges. The lower thermal contraction of the Ti-6Al-4 V wedges with respect to the stainless-steel clamp compensates for the larger thermal contraction of the winding pack compared to the stainless-steel coil former, thereby ensuring that the room temperature pre-load is maintained during cooldown, while simultaneously preventing a radial gap from occurring. A limited room temperature pre-load of 15 MPa is sufficient. The 'flexible' stainless-steel ring acts like a rope around the coil, thereby ensuring that the resulting radial pre-loads are the highest at the corners of the winding pack, where the magnetic flux density, and therefore the Lorentz loads, are also maximal.

The maximum radial magnetic field on the flutter coil during testing in self-field is 2.7 T at the outer pancake edges, while the maximum axial magnetic field is 4.0 T at half the coil height at the inner surface of the winding pack. The (limiting) peak radial magnetic field during operation of the flutter

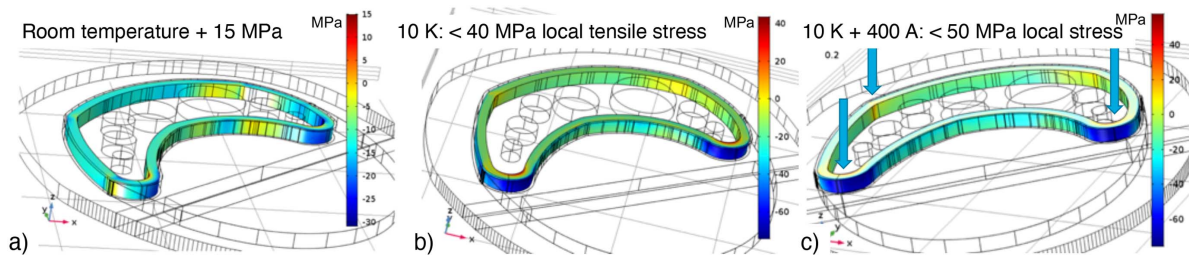


**Figure 12.** COMSOL<sup>®</sup> thermo-mechanical model of the tensile stresses in the windings along the conductor direction at room temperature with 15 MPa pressure on the coil former (a), after cooldown to 10 K (b), and after excitation of the coil to 400 A (c). The winding pack is modeled as a single unit with anisotropic properties. The maximum tensile stresses approaching 50 MPa occur at the inside of the winding pack at the sharpest-bend locations, as indicated by the arrows in (c).

coil in a compact cyclotron increases to 4.6 T at the outer pancake edges.

COMSOL<sup>®</sup> analyses of the von Mises stresses (figure 11, top) were performed a) at room temperature with 15 MPa preload, b) after cooldown to 10 K, and c) after cooldown at a current of 400 A, which is somewhat above the expected critical current in self-field. Simultaneously, the occurrence of a radial gap between the winding pack and the coil former was analyzed, as shown in the lower parts of figure 11. It is seen that the occurrence of a gap during cooldown and operation is indeed prevented by the clamp structure, apart from small local gaps at the corners that are at least partly due to the boundary conditions in the model. A local stress concentration was detected during the modeling, as indicated by the arrow in the top half of figure 11(a). A stainless-steel cylinder was embedded in the final test structure (section 4.5) to support the coil former in this location and prevent this stress concentration.

For the beam optics, it is important that the flutter coils have ‘sharp tips’, but the curvature in these locations is limited by the bending-strain that the conductor can sustain at room temperature. The tensile strain along the conductor path is calculated using the COMSOL<sup>®</sup> model to find out how the clamp structure and test add to the strain-state of the conductor in these locations. The results of these calculations are shown in figure 12 for the same circumstances as in figure 11.

The maximum tensile strain that is calculated in the winding pack occurs after cooldown and coil excitation at the inner radius of the sharpest bends in the winding pack and amounts to just under  $\sigma_t = 50$  MPa. Using the calculated Young’s modulus for the winding pack along the winding direction of  $E_t = 90$  GPa, the resulting tensile strain  $\epsilon_t$  that occurs in the winding pack of  $\epsilon_t = \sigma_t/E_t \times 100\% = 0.06\%$ , which is added to the bending strain. The bending strain  $\epsilon_b$  is, for a conductor thickness  $t$  and a bending diameter  $d$ , equal to  $\epsilon_b = t/d = 0.271/70 \times 100\% = 0.39\%$ . This is far enough below the yield strain of hard rolled stainless-steel 304 at room temperature (see table 2) to allow for some margin for the (not further specified) pre-tension with which the lamination is soldered to the DI-BSCCO Type H base-conductor. The total tensile strain at the outer fibers of the innermost tape-conductor is therefore on the order of 0.45%, which again is sufficiently below the low-temperature yield-strain of hard-rolled stainless-steel 304 (table 2). We conclude that the conductor will not be damaged by the additional tensile strain that results from the test.

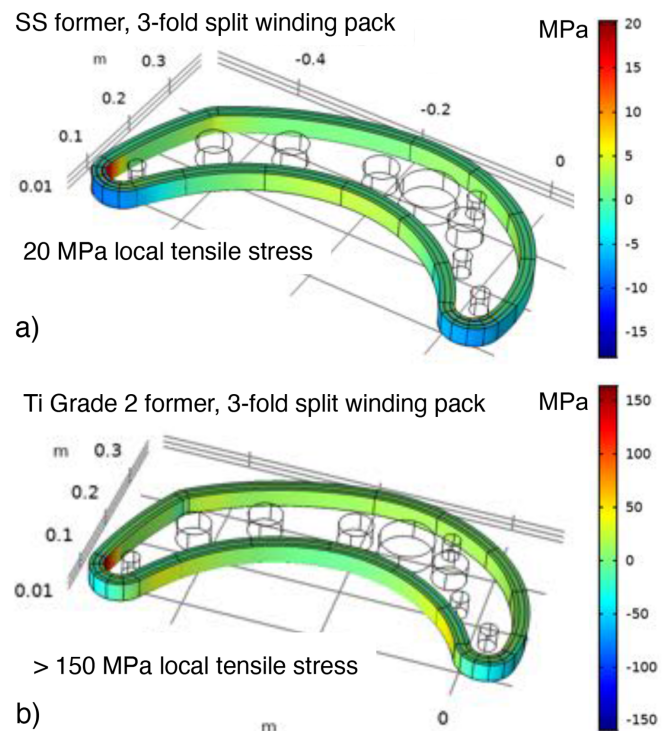


**Figure 13.** Comsol<sup>®</sup> thermo-mechanical model of the tensile stresses in the windings along the conductor direction after cooldown to 10 K, and using a radially three-fold split winding pack. The calculations were performed for a stainless-steel 316 L coil former (a) and for a titanium Grade 2 coil former (b).

It is important to note that for the results shown in figure 12, the winding pack is treated as a solid bar with anisotropic properties. In reality, one can argue whether the winding pack will ‘stick together’ or whether delamination will occur, rendering the individual turns to separate: Although the double pancakes are impregnated with epoxy, the tape-to-tape bonding between the polyimide insulated conductors can be expected to be weak. To determine the effect of de-bonding between the individual turns on the calculated tensile stress, a simulation was performed in which the winding pack was treated as three separate, non-bonded bars with anisotropic properties. The resulting tensile stresses in the winding pack for these calculations is shown in figure 13(a). It is found that the maximum tensile stress is reduced to 20 MPa (as opposed to 40 MPa in

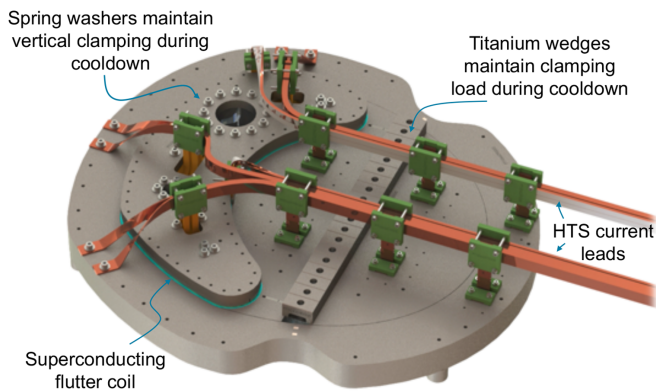


**Figure 14.** Stainless-steel 304 clamping structure with Ti-6Al-4 V wedges to maintain a 15 MPa radial pre-compression during cooldown, INCONEL<sup>®</sup> 718 Belleville spring-washers to retain vertical clamping on the winding pack during cooldown, and high purity copper busbars, which are shunted with REBCO tape for cooling and current transport.

the solid-bar calculation) after cooling down to 10 K, as a result of the de-bonding of the winding pack into three sections of equal thickness. Treating the winding pack as a solid-bar is therefore a worst-case calculation.

A further simulation was performed to find out whether a coil former with a lower thermal contraction could be used to prevent gaps between the coil former and the winding pack during cooldown. Calculations were performed for a titanium Grade 2 coil former. This material was selected in favor of Ti-6Al-4 V, because it has a similarly low thermal contraction during cooldown, but a higher thermal conductivity at low temperatures. The result of the calculations for a 3-fold split winding pack is shown in figure 13(b). It is found that the tensile stress, due to stretching of the winding pack around the low thermal contraction coil-former, has increased to an unacceptably high 150 MPa, and for a solid bar winding pack this value will be still significantly higher. Since conductor damage will occur in this configuration, the conclusion is that a higher thermal contraction coil-former, such as stainless-steel, needs to be used to prevent conductor damage, and gaps need to be closed by a surrounding structure.

#### 4.5. Conduction-cooled test

Since the detailed simulations highlight the need for a clamp structure for low-temperature tests, both to close all gaps and also to support the coil (and specifically the concave section) against Lorentz-loads, such a structure was designed and fabricated. The resulting clamp is shown in figure 14. Depicted are the radial clamp-structure with the Ti-6Al-4 V wedges for applying and retaining the 15 MPa pre-load. In the axial direction, the windings are supported by cover plates, with a separated section that is loaded with Belleville spring-washers to compensate for the larger axial contraction of the windings compared to the coil former, and in this way maintain a positive pressure on the winding pack during cooldown.

A stainless-steel cylinder is inserted in the largest hole in the coil former to provide support against the local high von

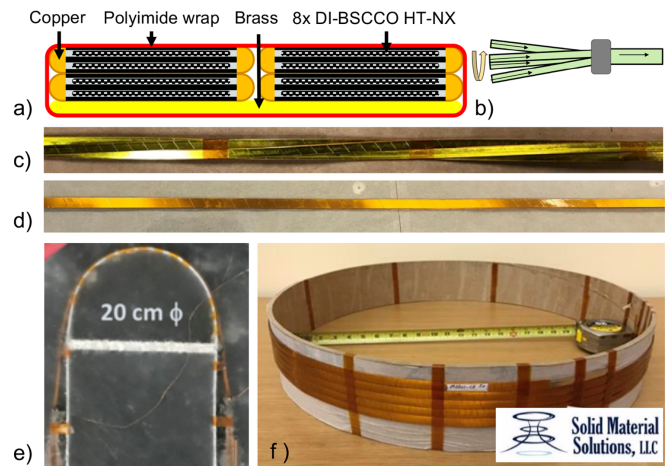


**Figure 15.** Transposed Bi-2223 cable developed for a cyclotron main coil. (a) Schematic of the cable cross-section used. (b) Machine cabling principle. (c) Transposed tape bundles before consolidation. (d) Consolidated cable. (e) Cable under bend test. (f) 9.5 meter machine-fabricated Bi-2223 cable for the main coil technology demonstrator.

Mises stress due to the pre-load, as highlighted by the arrow in figure 11(a). Large cross-section high-purity copper busbars are shown in figure 14 that are on one side connected to the cold heads, and on the other side to the clamp structure. These busbars are also connected to copper sleeves inside the holes in the coil former to provide direct cooling to the copper cooling-plates that are located in between the individual double-pancakes in the flutter coil. Parts of the busbars are used to transport the current to the coil, and these sections are shunted with REBCO HTS tapes.

The completed structure is placed inside a large conduction-cooled cryostat. Although such a cryostat was recently commissioned at Varian [38], we chose to perform the first flutter coil tests down to 20 K at the University of Twente in Enschede in the Netherlands. The reason for this is that the University of Twente, together with ECO 5, have gained a large experience with conduction-cooled tests of HTS coils during the EcoSwing program [41]. This experience is therefore utilized to more efficiently perform the important first tests, while at the same time reducing risk.

To further mitigate the risk when testing a new coil-configuration in a new test-environment, a first test-run will be performed using a single Bi-2223 double-pancake. The single double-pancake test is intended to be eventually destructive, by balancing the energy extraction-rate against the quench-detection voltage-level, which for DI-BSCCO coils appears to behave according to a generic pattern [42]. Driving the single double-pancake eventually to a destructive quench might provide insight on when damage to the flutter coil will start to occur on the generic quench balance behavior, thereby enabling prevention of quench damage to the flutter coil. The single double-pancake coil will after the test be used to obtain cut-outs of the winding pack to verify the calculated mechanical properties.

Tests are planned to start at 77 K to reproduce the liquid nitrogen results from SEI, after which the temperature will be stepped down, while at each step a critical current measurement will be performed with increasing current and stored energy. At the time of writing, the clamp system is being assembled and further test-preparations are carried out at the University of Twente. Test results will be published in a following article.

#### 4.6. Compact superconducting main coils

**4.6.1. Development of a transposed Bi-2223 cable.** Next to superconducting flutter coils, a compact isochronous cyclotron will also need higher performance main coils with a diameter on the order of 1 m, and generating a central magnetic field on the order of 5 T [38], i.e. around 7 T on the windings. For this, one could select a pre-reacted Nb<sub>3</sub>Sn cable, but the higher operating temperatures of HTS provides many cooling advantages, provided it can be produced with a suitable design and at a competitive price-point. The large temperature margins of REBCO (figure 8) are certainly attractive, but existing REBCO cable configurations seem at present not at a sufficiently low price-point for a cyclotron that needs to be series-produced at competitive cost. A second issue is that only a limited amount of current can be brought from room-temperature into a conduction-cooled cryostat, and the high performance of REBCO either yields a large cable that has too much current-carrying capacity, or too small a cable for a 1 m diameter solenoid.

Solid Material Solutions (SMS) investigated whether or not an affordable HTS cable with a suitable price-performance balance for 10 K, 7 T operation in a coil in a conduction-cooled environment, could be developed. SMS utilized the large strain-space that is available for SEI's DI-BSCCO HT-NX<sup>®</sup> tape [26] to develop a new transposed Bi-2223 cable configuration, named Magnum-NX<sup>®</sup>. A schematic cross-section of an early prototype version of this cable, as developed for Varian, is shown in figure 15(a).

The cable is comprised of four bundles of two tapes each, which are transposed during cabling as schematically shown in figures 15(a) and (b), with the photograph of figure 15(c) showing its structure after cabling. In the final step, the transposed cable of bundles is assembled and consolidated by placing a strip, in this case brass, on the top and/or bottom, with a polyimide overwrap resulting in the cables seen in figures 15(d) and (f). The Magnum-NX<sup>®</sup> cable was tested for bend tolerance as shown in figure 15(e), demonstrating that it allows for bending down to 20 cm diameter, without loss of current carrying capacity [43].

**4.6.2. Main coil technology testing.** To enable rapid testing of prototype superconducting technologies for a future main coil for a compact cyclotron, a compact conduction-cooled test-system for small-diameter solenoids was developed. This compact test-environment consists of a solenoid coil-former (figure 16(a) and (b)), and a small conduction-cooled vacuum

cryostat, with a dedicated Gifford-McMahon cryocooler (figure 16(c) and (d)). This removes the need to cool down the large conduction-cooled test-environment [38], and by creating small-scale coils in which all the required, but scalable, coil-technologies such as lead-in, lead-out, and a layer-transition can be demonstrated, we can test various configurations at low cost and with a high throughput. The added advantage of a small-scale test-environment is that only short conductor-lengths are required to demonstrate a certain conductor technology.

The small cryostat is designed to be as flexible as possible in terms of cooling options to accommodate multiple test scenarios. The main cooling is provided by the two-stage cryocooler, but the current leads are also equipped with a liquid nitrogen heat-exchanger to provide additional cooling-power at the current feed-throughs for high-current capacity cables. At present, this liquid-nitrogen cooling at the current feed-throughs limits the temperature range to which a coil can be tested, but further modifications can easily be implemented due to the manageable size of the system.

A prototype-length of the Magnum-NX<sup>®</sup> cable will be tested in the small main-coil test environment, in a coil with an inner diameter of the windings of 28 cm. Extensive bending-tests on the early-prototype Magnum-NX<sup>®</sup> cables indicated that in rare cases the inside brass-strip can buckle. To prevent this from happening in the small prototype-coil, the inside brass-strip was removed (as sketched in the cross-section in figure 15(a)). This compromise enables an early main-coil test with the Magnum-NX<sup>®</sup> prototype cable, even while the cable development has not yet fully matured. A number of >2 m length cable sections and a 9.5 m length section for the demonstrator coil (figure 15(f)) have so far been delivered to Varian, and the preparations for the coil test are presently ongoing. The 9.5 m cable length enables a two-layer, four turns-per-layer coil, with an inner diameter of the windings at 28 cm and a height of 65 mm. All the individual turns of the coil have been modelled in 3D Computer Aided Design in SOLIDWORKS<sup>®</sup>, so the pitch-reversal and the layer-jump are clear at forehand. This enables an accurate location of the cable-turns through the use of 3D-printed filler-pieces that are made from glass-fiber filled epoxy, which significantly simplifies coil winding.

In order to make accurate comparisons between the critical current of a Bi-2223 tape, a cable manufactured from such a tape, and a coil made from such a cable, self-field corrections have to be made for all three configurations. Since critical current data in the relevant temperature range for our foreseen tests between 60 K and 77 K is not readily available for the DI-BSCCO HT-NX<sup>®</sup> tape from which the Magnum-NX<sup>®</sup> cable is manufactured, we start the analyses using suitable data in the temperature range of interest from an older generation Bi-2223 conductor [43]. The original critical current density data in  $\text{kA}(\text{cm})^{-2}$  is scaled by a factor of 16.5 to arrive at the measured critical current in self-field of around 200 A for DI-BSCCO HT-NX<sup>®</sup> tape at 77 K [26]. These  $I_c(B \perp \text{tape})$  data at various temperatures are shown as open symbols in figure 17.

As a result of the steep initial reduction of the critical current of Bi-2223 with low magnetic fields perpendicular to the tape (see figure 8), it is prudent to apply self-field corrections

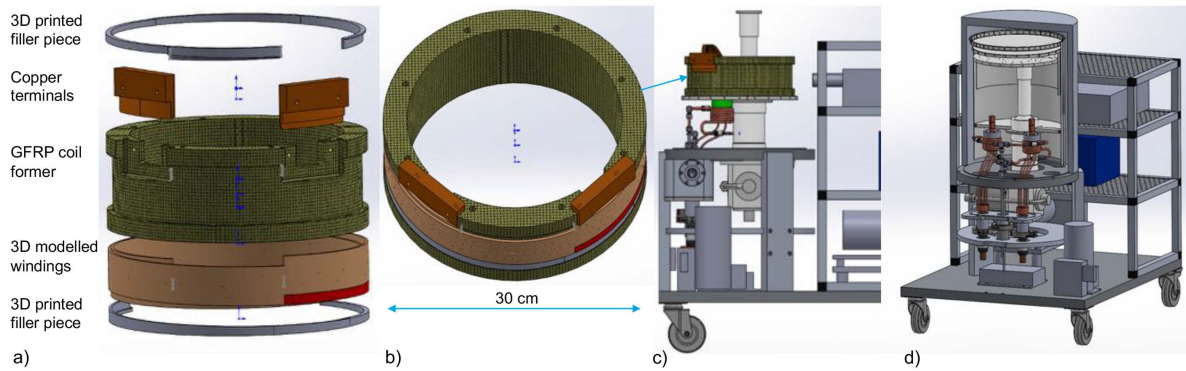


**Figure 16.** Main coil technology demonstrator with (a) an exploded view of the 30 cm coil, (b) a view of the assembled coil, (c) a view of the coil mounted in a small conduction-cooled test stand, and (d) a cut-open view of the complete small test stand in which also the liquid nitrogen cooled current-leads are visible.

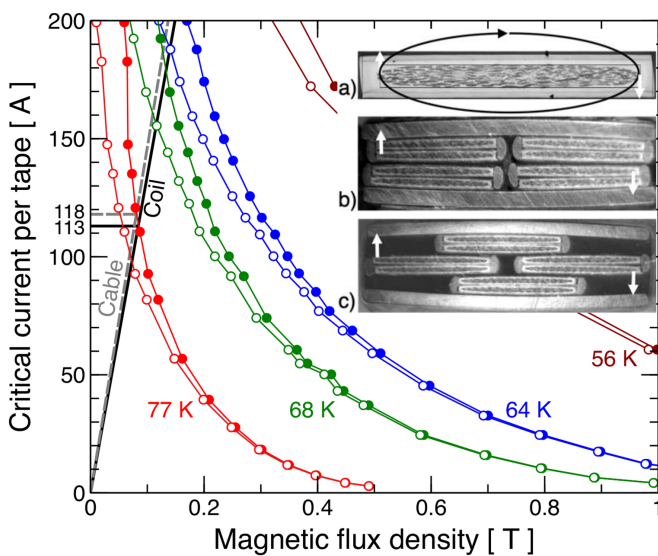


**Figure 17.** Critical current of Bi-2223 tapes as a function of magnetic flux density at relevant temperatures. Shown are the scaled as-measured data [43] in open symbols and the self-field corrected data as closed symbols. Also included are the load-lines of the cable and the technology demonstrator coil, scaled to the tape critical current. In the inset, the maximum field in the filaments and perpendicular to the tape is indicated for (a) a tape, (b) a cable cross-section, and (c) a cable cross-section half a twist pitch further along the cable.

to critical-current measurements on tape samples. This is similar to what is now commonly accepted practice for critical-current measurements on low-temperature superconducting wires such as Nb<sub>3</sub>Sn [44]. In order to make self-field corrections, the maximum perpendicular magnetic field component on the superconductor fraction in the tape cross-section that is generated by the current that the conductor is carrying needs to be calculated, at the location that is highlighted with white arrows in the inset in figure 17(a). To do this, the superconducting filament-area is approximated by a rectangular box of 0.152 mm height and 4.030 mm width, and the maximum perpendicular magnetic field is calculated at the middle of the small side of this box using a Microsoft® Excel spreadsheet,

**Table 3.** Maximum magnetic field in the superconducting cross-section and perpendicular to the tape, and expected cable and coil critical currents at 77 K based on the tape measurements.

	Tape	Cable (b/c)	Coil
Maximum field [ mT/A ]	0.246 8	0.683 3/0.601 9	0.743 7
Expected $I_c$ [ A ]	—	944	904

called SOLENO, and running a Visual Basic script that was developed at the University of Twente [45] for calculating the magnetic field around rectangular conductors. The resulting self-field correction is given in table 3, and the self-field corrected data are shown as closed symbols in figure 17.

For the Magnum-NX® cable, two cross-sections from an early prototype cable are considered that are separated by half a twist-pitch, as shown in the inset of figure 17(b) and (c). The maximum magnetic field in the cable at the location of the white arrows is calculated through summation of the magnetic-field contributions from the current flowing in the superconducting filament-areas in each of the individual tapes in the cross-section, while the areas, as above, are approximated as rectangles, and a homogeneous current-distribution is assumed. The resulting self-field corrections for the cable are summarized in table 3. The cable cross-section b) in figure 17 has the highest self-field and will therefore be limiting the cable performance when no external magnetic field is applied.

For the maximum magnetic field that is generated by the solenoid coil perpendicular to the tapes in the cable, the same SOLENO code is used to calculate the maximum radial magnetic field in the coil at half the coil thickness, and at 0.5 mm from the edge of the winding pack. Although this is not strictly speaking at the location of the superconducting fraction in the winding pack cross-section for a two-layer, four-turns-per-layer coil, it is sufficiently close, and the self-field is therefore calculated within the accuracy of the approximations. The resulting self-field for the coil is also given in table 3.

The load-lines of the cable and coil, calculated from the self-field values and normalized to the current per tape, i.e. divided by 8, are shown in figure 17, and their intersects with the self-field corrected tape data at 77 K forms a prediction

of the critical current that is expected for the cable and the coil without externally applied magnetic field. These expected critical-current values are also summarized in table 3. The critical current at 77 K from an actual measurement of a cable section is 1,070 A [43], i.e. 126 A more than as predicted. This difference can be attributed to margins in the assumptions of the parameters that are used for the calculations, a difference between the  $I_c(B \perp \text{tape})$  dependence of older-generation Bi-2223 conductor from a different manufacturer, or simply due to the tapes in the cable having a higher critical current than 200 A per tape at 77 K in self-field.

## 5. Conclusions

We have discussed a range of new technology developments to investigate the potential of using superconductors to enable more compact proton therapy systems based on an isochronous cyclotron. From comparisons of magnet complexity versus possible size reductions in gantries, and allowing for sufficient space in cyclotrons for the system to be realized on a space-constrained technical level, it becomes clear that a target magnetic field in the range of 5 to 7 T is the most appropriate. Balancing the desire to design cryogen-free systems against cooling-efficiency considerations and conductor performance yields an operating temperature of around 10 K.

Through considerations on ease of implementation, cost, performance, and conductor availability we find that, at least at present, Bi-2223 has the most desirable properties, while pre-reacted  $\text{Nb}_3\text{Sn}$  is a suitable alternative, for example for a cyclotron main coil. A combination of both can certainly also be considered.

We would like to stress that this is the status today, and future changes in the conductor landscape could change our present conclusion, specifically if, or when, the cost of REBCO will come down. We also would like to emphasize that magnets can obviously be made to work with the alternative conductors as well, e.g. (flutter) coils from REBCO or even  $\text{MgB}_2$ , so that there is not an unambiguous best solution, but preferred options that stem from our design considerations and boundary conditions.

The recently developed Magnum-NX<sup>®</sup> Bi-2223 cable broadens the application range for Bi-2223, specifically for larger coils. The cable can be fabricated at a highly competitive price-point, but further developments will be needed to arrive at a commercial product that has an optimized critical current density and that includes solutions to handle the transverse loads that will be present in any high-performance magnet system.

In terms of the implementation of superconductivity in the various magnets and coils that are needed for proton therapy systems, we find that for gantry bend magnets the reduction in gantry diameter is not dramatic. Other technology changes will therefore have to be made as well, which can be combined with superconducting technology to arrive at truly compact treatment systems. Our efforts so far have shown that curved dipoles will not be easy to fabricate. When gantries will become more compact, the dipoles will need to be curved

more, and stray magnetic fields closer to the imaging system and patient will also need to be handled.

The need for superconducting flutter coils to enable more compact isochronous cyclotrons represents a major hurdle, but we have shown that in principle these complex-shaped coils can be produced. It should be emphasized though, that there are 16 flutter coils required for a four-fold symmetry isochronous cyclotron, and that a large series production of such coils at an acceptable price-point requires further optimizations of the technology.

Implementation of superconductivity in the main coils of a cyclotron has already been demonstrated since long. The question therefore is how to drive this further towards more compact and higher-field systems that are ideally cryogen-free. Naturally, the optimal conductor for a, say, 1 m diameter split solenoid, will be a cable. Both the Magnum-NX<sup>®</sup> cable as well as a pre-reacted  $\text{Nb}_3\text{Sn}$  cable seem attractive options. A key complication for cryogen-free systems will be to bring the high current for a high-performance cable from room temperature into the low-temperature coil. Clearly, a balance between the desire for a large cable (ease of winding and low inductance) and cooling capacity at the current entrance-point will need to be found.

Our overall conclusion is that in order to arrive at truly compact proton treatment facilities, superconducting technologies will be required, in combination with further developments in other technology areas. When observing the need that exists for affordable proton treatment systems, then the use of superconductivity in particle therapy applications can become a new and large commercial application of superconductors, next to magnets for Medical Resonance Imaging and Nuclear Magnetic Resonance.

## Acknowledgments

This work was partly funded by the European Regional Development Fund (ERDF) under contract number EFRE-0800942. Varian would like to thank C Calzolaio, A Gerbershagen, A Lomax, D Meer, K Nesteruk, S Sanfilippo, M Schippers, M Seidel, and C Zoller at the Paul Scherrer Institute in Switzerland, and L Brouwer, R Hafalia, H Higley, A Hodgkinson, S Prestemon, J Swanson, and W Wan at Lawrence Berkeley National Laboratory in the USA for their valuable contributions in studies on superconducting bend magnets for gantries. The work at Lawrence Berkeley National Laboratory was supported by the U.S. Department of Energy under Contract No. DE-AC02-05CH11231.

## ORCID iDs

A Godeke  <https://orcid.org/0000-0002-8924-9878>  
H Röcken  <https://orcid.org/0000-0003-0379-8698>  
A Nijhuis  <https://orcid.org/0000-0002-1600-9451>

## References

- [1] Garcia M, Jemal A, Ward E M, Center M M, Hao Y, Siegel R I and Thun M J 2007 *Global Cancer Facts & Figures 2007* (Atlanta, GA: American Cancer Society)
- [2] 2018 *Global Cancer Facts & Figures 4th edn* ed (Atlanta, GA: American Cancer Society)
- [3] Alonso J R and Antaya T A 2012 *Rev. Accel. Sci. Techn.* **5** 227–63
- [4] Particle Therapy Co-Operative Group 2019 ([www.ptcog.ch/index.php/facilities-in-operation](http://www.ptcog.ch/index.php/facilities-in-operation))
- [5] Ferracin P et al 2009 *IEEE Trans. Appl. Supercond.* **19** 1240–3
- [6] Rossi L 2004 *IEEE Trans. Appl. Supercond.* **14** 153–8
- [7] Varian Medical Systems Flash Forward™ Consortium (<https://www.varian.com/oncology/solutions/proton-therapy/flashforward-consortium>)
- [8] Calzolaio C, Sanfilippo S, Calvi M, Gerbershagen A, Negrazus M, Schippers M and Seidel M 2016 *IEEE Trans. Appl. Supercond.* **26** 4401005 5pp
- [9] Sanfilippo S, Calzolaio C, Anghel A, Gerbershagen A and Schippers J M 2016 Conceptual design of superconducting combined-function magnets for the next generation of beam cancer therapy gantry *Proc. of RuPAC2016* (St. Petersburg, Russia) p THCDMH01
- [10] Gerbershagen A, Meer D, Schippers J M and Seidel M 2016 *Zeitschrift für Medizinische Physik* **26** 224–37
- [11] Gerbershagen A, Calzolaio C, Meer D, Sanfilippo S and Schippers M 2016 *Supercond. Sci. and Techn.* **29** 083001 15pp
- [12] Nesteruk K P, Calzolaio C, Meer D, Rizzoglio V, Seidel M and Schippers J M 2019 *Phys. Med. Biol.* **64** 175007
- [13] Wan W, Brouwer L, Caspi S, Prestemon S, Gerbershagen A, Schippers J M and Robin D 2015 *Phys. Rev. ST Accel. Beams* **18** 103501 23pp
- [14] Brouwer L N 2015 Canted-Cosine-Theta Superconducting Accelerator Magnets for High Energy Physics and Ion Beam Cancer Therapy *Ph.D. thesis* (Berkeley: University of California)
- [15] Brouwer L, Caspi S, Hafalia R, Hodgkinson A, Prestemon S, Robin D and Wan W 2017 *IEEE Trans. Appl. Supercond.* **27** 4400106 16pp
- [16] Brouwer L et al 2019 *Nucl. Instr. and Methods in Phys. Res. Section A* **957** 163414 18pp
- [17] Spiller P, Boehne D, Dolinskii A, Eickhoff H, Franczak B, Langenbeck B, Haberer T, Malwitz E and Pavlovic M 2000 Gantry studies for the proposed heavy ion cancer therapy facility in Heidelberg *Proc. of EPAC2000* (Vienna, Austria)
- [18] Iwata Y et al 2018 Superconducting Gantry for Carbon-Ion Radiotherapy *Proc. 9th Int. Particle Conf. (IPAC'18), Vancouver, BC, Canada, April 29-May 4, 2018 (Int. Particle Conf. no 9)* (Geneva, Switzerland: JACoW Publishing) pp 1232–6
- [19] Trbojevic D, Parker B, Keil E and Sessler A M 2007 *Phys. Rev. ST Accel. Beams* **10** 053503 6pp
- [20] Derenchuk V P 2017 *Application of Superconducting Technology for Proton Therapy Presented at Napac 2016* (Chicago, IL, USA) unpublished
- [21] ITER Conductor production phase parameterization on unpublished data for Luvata ITER quality Internal Tin wire
- [22] Godeke A, ten Haken B, ten Kate H H J and Larbalestier D C 2006 *Supercond. Sci. and Techn.* **19** R100–R116
- [23] Bottura L and Bordini B 2009 *IEEE Trans. Appl. Supercond.* **19** 1521–4
- [24] Kitaguchi H 2010 Private Communication
- [25] Kitaguchi H, Takahashi K, Kumakura H, Hayashi T, Fujino K, Ayai N and Sato K 2009 *Supercond. Sci. and Techn.* **22** 045005 8pp
- [26] Godeke A et al 2017 *Supercond. Sci. and Techn.* **30** 035011 15pp
- [27] Francis A 2019 Critical current data for overpressure reacted Bi-2212 wire measured for the NHMFL NMR magnet program Private communication
- [28] Abraimov D V 2017 Critical current data on Superpower REBCO tapes measured for the NHMFL 32 T magnet program Private communication
- [29] Leroy D, Oberli L, Perini D, Siemko A and Spigo G 1998 Design features and performance of a 10 T twin aperture model dipole for LHC *Proc. of the 15th International Conference on Magnet Technology* (Beijing, China) Liangzhzen L, Guoliao S and Lugang Y vol 1 pp 119–22 (Beijing, China: Science Press)
- [30] Bottura L 2000 *IEEE Trans. Appl. Supercond.* **10** 1054–7
- [31] Baumgarten C, Geisler A, Klein U, Krischel D, Röcken H, Schillo M, Stephani T and Timmer J H 2007 *Nucl. Instrum. Methods Phys. Res. A* **570** 10–4
- [32] Godeke A, Turrioni D, Boutboul T, Cheggour N, Ghosh A K, Goodrich L F, Meinesz M and den Ouden A 2009 *IEEE Trans. Appl. Supercond.* **19** 2633–6
- [33] Larbalestier D C et al 2014 *Nat. Mater.* **13** 375–81
- [34] Godeke A et al 2010 *Supercond. Sci. and Techn.* **23** 034022 6pp
- [35] Godeke A, Hartman M H C, Mentink M G T, Jiang J, Matras M, Hellstrom E E and Larbalestier D C 2015 *Supercond. Sci. and Techn.* **28** 032001
- [36] Oguro H, Watanabe K, Awaji S, Hanai S, Ioka S, Sugimoto M and Tsubouchi H 2016 *Supercond. Sci. and Techn.* **29** 084004
- [37] Hatanaka K, Fukuda M, Hamatani N, Izumi T, Kamakura K, Saito T, Ueda H, Yasuda Y, Yorita T and Kawaguchi T 2012 *Development of HTS Magnets IPAC2012 Proc., TUOAC02* 1095
- [38] Akcöltekin E, Alberty L, Bergmann C, Busold C, Fritz S, Godeke A, Klarner F, Nast R, Radermacher C, Röcken H, vom Stein P, Walpole M and Wittschen J Design studies for a compact isochronous 224 MeV medical cyclotron using HTS technology To be published
- [39] COMSOL Multiphysics®, ([www.comsol.com](http://www.comsol.com)), COMSOL AB, Stockholm, Sweden
- [40] Battelle Columbus Laboratories, Ohio 1977 *Handbook on materials for superconducting machinery* (Springfield, VA: National Technical Information Service, U.S. Department of Commerce) 22161
- [41] Bergen A et al 2019 *Supercond. Sci. and Techn.* **32** 12500612 pp
- [42] Yamaguchi T, Ueno E, Kato T and Hayashi K 2015 *Physics Procedia* **65** 225–8
- [43] Otto A, Saraco L, Colque J and Pothier III G 2018 Rutherford cable made with Sumitomo type NX 1G tape presented at the 2018 *Appl. Supercond. Conf.* (Seattle, WA, USA) presentation 4Lor2C-04
- [44] Godeke A, Chlachidze G, Dietderich D R, Ghosh A K, Marchevsky M, Mentink M G T and Sabbi G L 2013 *Supercond. Sci. and Techn.* **26** 095015 15pp
- [45] Krooshoop H J G and Mulder G University of Twente SOLENO Visual Basic Script for magnetic field calculations for solenoid and rectangular conductors Private communication